Published in Eur. Phys. J. E **39**, 54 (2016)
DOI 10.1140/epje/i2016-16054-1

arXiv:1607.01131v1 [cond-mat.soft] 5 Jul 2016

Transport and selective chaining of bidisperse particles in a travelling wave potential

Pietro Tierno[1,2] and Arthur V. Straube[1]

[1] Departament de Física de la Matèria Condensada, Universitat de Barcelona, Av. Diagonal 647, 08028 Barcelona, Spain
[2] Institut de Nanociència i Nanotecnologia IN^{2}UB, Universitat de Barcelona, Barcelona, Spain

Abstract. We combine experiments, theory and numerical simulation to investigate the dynamics of a binary suspension of paramagnetic colloidal particles dispersed in water and transported above a stripe patterned magnetic garnet film. The substrate generates a one-dimensional periodic energy landscape above its surface. The application of an elliptically polarized rotating magnetic field causes the landscape to translate, inducing direct transport of paramagnetic particles placed above the film. The ellipticity of the applied field can be used to control and tune the interparticle interactions, from net repulsive to net attractive. When considering particles of two distinct sizes, we find that, depending on their elevation above the surface of the magnetic substrate, the particles feel effectively different potentials, resulting in different mobilities. We exploit this feature to induce selective chaining for certain values of the applied field parameters. In particular, when driving two types of particles, we force only one type to condense into travelling parallel chains. These chains confine the movement of the other non-chaining particles within narrow colloidal channels. This phenomenon is explained by considering the balance of pairwise magnetic forces between the particles and their individual coupling with the travelling landscape.

1 Introduction

Recent years have witnessed an increasing interest in developing novel techniques which make use of uniform magnetic field modulated by a periodic substrate in order to induce the controlled motion of colloidal microspheres in water [1,2,3,4,5,6,7,8]. In contrast to optical or electric field micromanipulation, magnetic fields have the advantages that they neither alter the fluid medium nor affect biological systems, although their use is limited to polarizable particles [9,10]. Magnetophoresis, *i.e.* the controlled transport of particles via an external field gradient, is a well established method with several applications in biomedical research and clinical diagnostics [11,12]. However, precise control of particle position and speed in a single chip is difficult to obtain with a field gradient since the amplitude varies spatially over an extended area.

Magnetic fields that are heterogeneous on the particle scale can guarantee a precise and selective manipulation of both individual and large collection of colloidal microspheres. Such fields can be obtained by using magnetic patterned substrates which contain, for example, permalloy islands [3], cobalt microcylinders [4], domain wall conduits [6], magnetic wires [7], or even exchange bias systems [8]. Another method consists in using ferrite garnet films (FGFs), *i.e.* epitaxially grown single crystalline films where magnetic domains organize into patterns of stripes with a spatial periodicity of few microns. These domains generate a one dimensional periodic potential which can be used to trap [13], assemble [14] or transport [15] paramagnetic colloidal particles deposited above the film. In the latter case, it was found that an external rotating magnetic field is able to create a moving landscape, similar to a travelling wave potential, which can transport the particles at a well defined speed [16]. In particular, depending on the driving frequency, two dynamic states are possible: (i) at low frequencies, the particles are synchronized with the external field and are therefore transported with the speed of the travelling landscape; (ii) beyond a critical value f_c, the particles desynchronize with the translating potential, showing a complex sliding dynamics characterized by a global decrease of their average speed. However, theoretical arguments [17] reveal that the transition between both states is strongly sensitive to the particle elevation above the substrate, opening the possibility to separate magnetic particles based on their relative size. This feature was already demonstrated in different works using similar [18,19], or different [20] magnetic substrates. However, the role of interparticle interaction in this process and their relative effect on the collective dynamics for a bidisperse colloidal system has not been explored so far.

In this article, we study the dynamics and interactions between paramagnetic colloidal particles transported above a travelling wave potential. We focus on a binary mixture where different elevation above the magnetic substrate modifies the particle collective behaviour under an applied field. In particular, an elliptically polarized magnetic field is used to induce strong attraction between one type of particle, triggering the formation of long chains

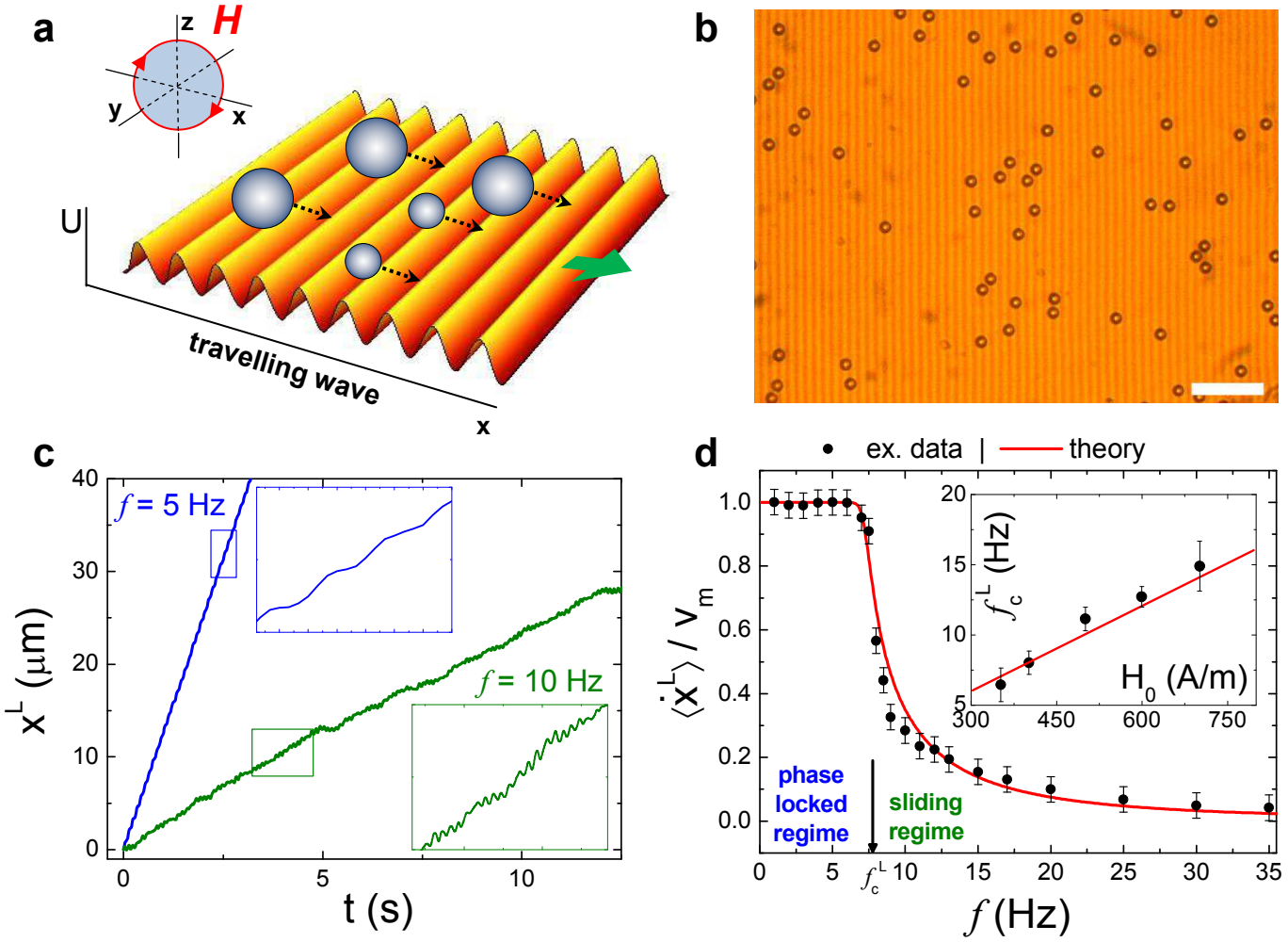

Fig. 1. (a) Schematic showing a binary mixture of paramagnetic colloidal particles transported above a travelling periodic energy landscape. The latter is induced by an external magnetic field rotating in the (x, z) plane. (b) Polarization microscope image showing the stripe patterned FGF (of spatial periodicity $\lambda = 2.6\,\mu$m) with a diluted sample of large (L) particles (diameter $d^{\rm L} = 2.8\,\mu$m). Scale bar is $20\,\mu$m. (c) Trajectory of one large particle driven across the FGF by an applied circularly polarized ($\beta = 0$) field with amplitude $H_0 = 400\,$A/m and at two frequencies $f = 5\,$Hz (blue, phase locked regime) and $f = 10\,$Hz (green, sliding regime). (d) Particle velocity $\langle \dot{x}^{\rm L} \rangle / v_{\rm m}$ normalized by the speed $v_{\rm m} = \lambda f$ of translation of the landscape as a function of driving frequency f for a large paramagnetic colloidal particle subjected to a rotating field with amplitude $H_0 = 400\,$A/m and ellipticity $\beta = 0$. Continuous line denotes the nonlinear fit following Eq. (8) in the text, while scattered points (filled circles) are experimental data. Inset shows the dependence of the critical frequency $f_{\rm c}^{\rm L}$ as a function of the field amplitude H_0.

travelling at constant speed along the corrugated potential. However, this chaining effect does not occur for the other colloidal species, which slides close to the moving chains. We explain this peculiar behaviour by using simple theoretical arguments, and confirm the observed dynamics via numerical simulations.

2 Experimental system

The substrate potential is generated by using an FGF of thickness $\simeq 4\,\mu$m grown by dipping liquid phase epithaxy [21]. The FGF is characterized by a stripe pattern of ferromagnetic domains having alternating magnetization with a spatial periodicity given by $\lambda = 2.6 \pm 0.2\,\mu$m, Fig. 1(b). These domains are separated by Bloch walls (BWs), *i.e.* transition regions where the magnetization vector rotates by 180 degrees out of the film plane, and the stray field of the film is maximal. Because of this arrangement of the magnetic domains, under no external field the FGF generates on its surface a static spatially periodic potential, which is characterized by a step-like profile directly at the surface of the FGF and a smoothed sinusoidal-like profile far away from the surface. We transport above the FGF two types of paramagnetic colloidal particles, having diameters $d^{\rm S} = 1.0\,\mu$m (Dynabeads my-

one, Dynal) and $d^{\mathrm{L}} = 2.8\,\mu$m (Dynabeads M-270, Dynal), and effective magnetic volume susceptibility $\chi^{\mathrm{S}} \simeq 1$ [22] and $\chi^{\mathrm{L}} \simeq 0.4$ [23], respectively. Hereafter, the superscripts "S" and "L" are used to refer to the small and large particles. Both types of particles are composed of a cross-linked polystyrene matrix doped with superparamagnetic iron oxide grains and coated with COOH surface groups. The particles are diluted with deionized water (milli-Q, Millipore) and deposited above the FGF, where they sediment due to density mismatch. Once close to the surface of the FGF, the particles are attracted to the BWs which confines their motion in two dimensions. In order to decrease the strong attraction of the BWs and avoid particle sticking, the FGF is coated with a $1\,\mu$m thick layer of a photoresist (AZ-1512 Microchem, Newton, MA) using spin coating and UV-photo crosslinking [24]. Thus the effective particle elevation above the surface of the FGF (*i.e.* the shortest distance from the surface of the FGF to the center of particle) is $z^{\mathrm{S}} = 1.5\,\mu$m and $z^{\mathrm{L}} = 2.4\,\mu$m for the small and large particle, respectively.

The particle dynamics are observed by using a polarization optical microscope (Eclipse Ni, Nikon) which is equipped with a $100\times$ 1.3 NA microscope objective and a 0.45 TV lens. The microscope has a CCD camera (Basler Scout scA640-74) which is capable of recording real-time video clips of the particles up to 75 frames/s in a total field of view of $140\times105\,\mu\mathrm{m}^2$. We extract the particle trajectories from these recorded data using a custom made tracking software based on the Crock and Grier original code [25]. The external field is applied by using a custom made magnetic coil system mounted on the stage of the optical microscope and connected to two independent power amplifiers (BOP 20 10-M, KEPCO) driven by an arbitrary waveform generator (TGA1244, TTi).

3 Theoretical model

Consider a mixture of spherical paramagnetic particles numbered by $l = 1, 2, 3, \ldots$. Because the particles are bidisperse, they are characterized by diameters $d_l = \{d^{\mathrm{S}}, d^{\mathrm{L}}\}$ and the effective volume susceptibilities $\chi_l = \{\chi^{\mathrm{S}}, \chi^{\mathrm{L}}\}$, as described in Sec. 2. A paramagnetic spherical particle l positioned at $\mathbf{r}_l$ and subjected to an external field $\mathbf{H}$ acquires a dipole moment $\mathbf{m}_l = V_l\chi_l\mathbf{H}_l$ [26], where $V_l = \pi d_l^3/6$ is the volume of particle and the field is taken at the position of particle, $\mathbf{H}_l = \mathbf{H}(\mathbf{r}_l, t)$. This dipole interacts with the external magnetic field and with other induced dipoles, say dipole l' at a position $\mathbf{r}_{l'}$, whose interaction potentials can be written as

$$U_{\mathrm{s}}(\mathbf{r}_l, t) = -\frac{1}{2}V_i\chi_l\mu_0\mathbf{H}^2(\mathbf{r}_l, t) = -\frac{1}{2}V_i\chi_l\mu_0\mathbf{H}_l^2, \quad (1)$$

$$U_{\mathrm{dd}}(\mathbf{r}_{ll'}, t) = \frac{\gamma_{ij}}{r_{ll'}^3}\left[(\mathbf{H}_l\cdot\mathbf{H}_{l'}) - 3(\mathbf{H}_l\cdot\hat{\mathbf{r}}_{ll'})(\mathbf{H}_{l'}\cdot\hat{\mathbf{r}}_{ll'})\right], \quad (2)$$

respectively. Here, $\mu_0 = 4\pi\times10^{-7}\,\mathrm{H\,m^{-1}}$ is the magnetic permeability of the free space, $\gamma_{ll'} = \chi_l\chi_{l'}V_lV_{l'}\mu_0/(8\pi)$, $\mathbf{r}_{ll'} = \mathbf{r}_l - \mathbf{r}_{l'}$, $r_{ll'} = |\mathbf{r}_{ll'}|$, and $\hat{\mathbf{r}}_{ll'} = \mathbf{r}_{ll'}/r_{ll'}$.

For our system, the magnetic field $\mathbf{H}$ is the total field above the FGF, given by the superposition $\mathbf{H} = \mathbf{H}^{\mathrm{sub}} + \mathbf{H}^{\mathrm{ac}}$ of the stray field of the substrate, $\mathbf{H}^{\mathrm{sub}}$, and the field of modulation, $\mathbf{H}^{\mathrm{ac}}$. To a good accuracy, the substrate field $\mathbf{H}^{\mathrm{sub}}$ can be approximated as [17]

$$\mathbf{H}^{\mathrm{sub}}(\mathbf{r}) = \frac{4M_{\mathrm{s}}}{\pi}\mathrm{e}^{-kz}\left(\cos kx, 0, -\sin kx\right), \quad (3)$$

where M_{s} denotes its saturation magnetization and $k = 2\pi/\lambda$ is the wavenumber. The superimposed ac field rotates in the (x, z) plane and has elliptic polarization:

$$\mathbf{H}^{\mathrm{ac}}(t) = (H_{0x}\cos\omega t, 0, -H_{0z}\sin\omega t), \quad (4)$$

where $\omega = 2\pi f$ is the angular frequency. The amplitude of modulation H_0 and the ellipticity parameter $\beta \in [-1, 1]$ are introduced as [27] $H_0 = \sqrt{(H_{0x}^2 + H_{0z}^2)/2}$ and $\beta = (H_{0x}^2 - H_{0z}^2)/(H_{0x}^2 + H_{0z}^2)$. The partial case of $\beta = 0$ corresponds to the case of circular polarization, $H_{0x} = H_{0z}$.

The dynamics of particles is considered overdamped and two dimensional, at a fixed elevation above the FGF, resulting in the following Langevin equations

$$\zeta_l\frac{d\mathbf{r}_l}{dt} = \mathbf{F}_{\mathrm{s}}(\mathbf{r}_l, t) + \sum_{l'}\mathbf{F}_{\mathrm{d}}(\mathbf{r}_{ll'}, t) + \sqrt{2\zeta_l k_{\mathrm{B}}T}\,\boldsymbol{\xi}_l(t), \quad (5)$$

where $\zeta_l = 3\pi\eta d_l$ is the viscous friction coefficient (η is the dynamic viscosity of the solvent), $\mathbf{F}_{\mathrm{s}}(\mathbf{r}_l, t) = F_{\mathrm{s}}(x_l, t)\hat{\mathbf{e}}_x$ ($\hat{\mathbf{e}}_x$ is the unit vector of the x axis), $F_{\mathrm{s}}(x_l, t) = -\partial_{x_l}U_{\mathrm{s}}(\mathbf{r}_l, t)$ is the force exerted on particle l by the external field, and $\mathbf{F}_{\mathrm{dd}}(\mathbf{r}_{ll'}, t) = -\partial_{\mathbf{r}_l}U_{\mathrm{dd}}(\mathbf{r}_{ll'}, t)$ is the dipolar force from particle l'. The last term in Eq. (5), in which $k_{\mathrm{B}}T$ is the thermal energy, is the stochastic force taking account of thermal fluctuations modelled by the Gaussian white noise with the mean and covariance given by $\langle\boldsymbol{\xi}_{l'}(t)\rangle = 0$ and $\langle\boldsymbol{\xi}_l(t)\boldsymbol{\xi}_{l'}(t')\rangle = \mathbf{I}\,\delta_{ll'}\delta(t - t')$, respectively. Here, $\mathbf{I}$ is the second-order identity tensor.

To account for the finite size of particles, we also include hard-core repulsive potential, as we did in Ref. [28].

4 Discussion

4.1 Individual particle propulsion for circular polarization

In the case of circular polarization, $\beta = 0$, the potential that describes the single particle motion, U_{s} as in Eq. (1), evaluated based on expressions (3) and (4) corresponds to a sinusoidal wave propagating with the speed $v_{\mathrm{m}}(f) = \lambda f$ across the stripes of the FGF, $U_{\mathrm{s}}(x_l, t) \propto \cos[k(x_l - v_{\mathrm{m}}t)]$. As a result, v_{m} is the maximum speed that the particles acquire when following the potential at low frequencies. This phase-locked motion is characterized by a constant propulsion speed, as confirmed by an almost linear particle trajectory shown by the blue line in Fig. 1(c). At high frequencies, particles decouple from the potential, moving in an asynchronous way with on average smaller speeds. Now the particles are in a sliding regime, displaying a

series of oscillations along their motion, see the green curve in Fig. 1(c). Both regimes of motion can be characterized in terms of the average propulsion speed, $\langle \dot{x}_l \rangle$, as shown in Fig. 1(c) for a single particle of size d^L.

It can be shown that the deterministic ($T = 0$) averaged speed of the particles can be derived as, [17]

$$\langle \dot{x}_l \rangle_{\beta=0} = v_\mathrm{m} \begin{cases} 1, & \text{if } f < f_{cl}(0)\,, \\ 1 - \sqrt{1 - f_{cl}^2(0)/f^2}\,, & \text{if } f > f_{cl}(0)\,, \end{cases} \quad (6)$$

where

$$f_{cl}(\beta = 0) = \frac{8 M_\mathrm{s} H_0 \mu_0 V_l \chi_l}{\zeta_l \lambda^2} \mathrm{e}^{-k z_l} \quad (7)$$

is the critical frequency, as denoted by the subscript "c". The subscript "l" indicates that the critical frequency is generally particle dependent since particles of different sizes are characterized by different values of the parameters V_l, χ_l, ζ_l, and z_l.

In contrast to a sharp transition displayed by the deterministic prediction, Eq. (6), the account of thermal fluctuations ($T > 0$) smoothens the crossover from the phase-locked to the sliding motion close to the critical point. Thus the effect of thermal noise on the average particle speed is described by

$$\langle \dot{x}_l \rangle_{\beta=0} = v_\mathrm{m} \left[1 - \frac{\sinh(\pi \alpha_l)}{\pi \alpha_l \, |I_{\mathrm{i}\alpha_l}(\alpha_{\mathrm{cl}})|^2} \right], \quad (8)$$

where $I_{\mathrm{i}\nu}(x)$ is the modified Bessel function of the first kind of an imaginary order, and we have introduced dimensionless parameters

$$\alpha_l = \frac{\zeta_l f \lambda^2}{2\pi k_\mathrm{B} T}\,, \quad \alpha_{cl} = \frac{\zeta_l f_{cl}(0) \lambda^2}{2\pi k_\mathrm{B} T}\,. \quad (9)$$

Equation (8) is used to fit the experimental data for the average speed $\langle \dot{x}_l \rangle$ for the large particles with $d_l = d^\mathrm{L}$ at $H_0 = 400\,\mathrm{A/m}$ against the theoretical predictions, see Fig. 1(d). We find that at this amplitude of the applied field, the critical frequency is given by $f_\mathrm{c}^\mathrm{L}(0) = 7.7\,\mathrm{Hz}$, which allow us to estimate the saturation magnetization $M_\mathrm{s} \approx 24600\,\mathrm{A/m}$, used as a fitting parameter. Note that the linear dependence of the critical frequency on the amplitude of modulation can be seen from the inset of Fig. 1(d), which is in accordance with the theoretical prediction given by Eq. (7).

We next show in Fig. 2 the normalized mean speeds as a function of frequency for particles with the diameters d^L and d^S and subjected to a rotating magnetic field with amplitude $H_0 = 400\,\mathrm{A/m}$. As expected, given the different values of the particle parameters, the smaller particles (d^S) require a much higher frequency barrier to desynchronize with the travelling potential and enter the sliding regime. The corresponding curve (empty circles in Fig. 2) can be well fitted by Eq. (8) using the same value of M_s, as in Fig. 1(d). We find the critical frequency for the small particles to be $f_\mathrm{c}^\mathrm{S} = 20.3\,\mathrm{Hz}$, which is so high that the average speed of the large particles has already decreased by 90%, $\langle \dot{x}^\mathrm{L} \rangle = 0.1\, v_\mathrm{m}$. This feature enables us to separate the paramagnetic particles based on the significant difference in their relative speeds, when driving both types of particles at a frequency above $f_\mathrm{c}^\mathrm{L} = 7.7\,\mathrm{Hz}$. For frequencies higher than 100 Hz the particles eventually slow down till to be practically unable to follow the quickly moving landscape. In contrast, below $f_\mathrm{c}^\mathrm{L} = 7.7\,\mathrm{Hz}$, both types of particles can be transported at the same constant speed, v_m, staying completely localized along a series of equipotential lines of the travelling potential, equally spaced and aligned along the stripes, as shown in the small inset in Fig. 2.

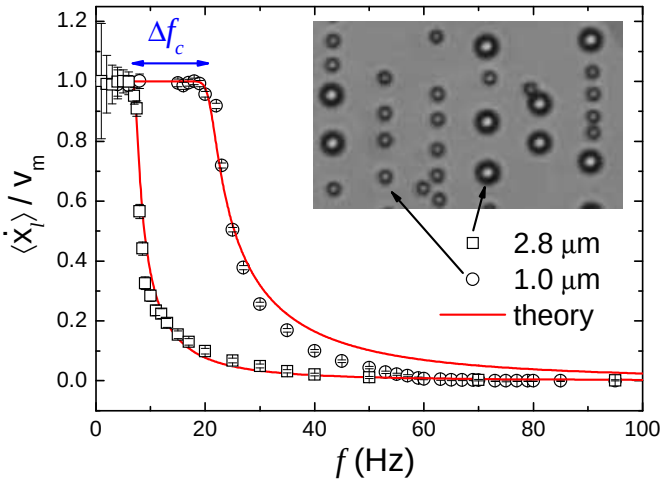

Fig. 2. Normalized particle velocity $\langle \dot{x} \rangle / v_\mathrm{m}$ (where $v_m = \lambda f$) as a function of the driving frequency f for a large (2.8 μm, empty squares) and small (1.0 μm, empty circles) paramagnetic colloidal particle subjected to a rotating field with amplitude $H_0 = 400\,\mathrm{A/m}$ and ellipticity $\beta = 0$. The continuous red lines are fits according to Eq. (8), and $\Delta f_\mathrm{c} = f_\mathrm{c}^\mathrm{S} - f_\mathrm{c}^\mathrm{L} = 12.6\,\mathrm{Hz}$ denotes the difference between the critical frequencies of the large (L) and the small (S) particle. Inset shows a microscope image of both kinds of particles above the FGF. The vertical stripes are not visible due to the absence of polarization elements.

4.2 Interacting particles for elliptic polarization. Reduced model

When transported by the travelling potential, the paramagnetic colloidal particles also interact with each other because of magnetic dipolar forces. It has recently been shown in a previous work [28] that these forces can be tuned by varying the ellipticity β of the rotating field. A pair of similar particles moving one behind another above the FGF display either repulsive or attractive interactions for an ellipticity parameter $\beta < \beta_\mathrm{c}$ or $\beta > \beta_\mathrm{c}$, respectively. Here $\beta_\mathrm{c} = -1/3$ denotes the transition between both types of behaviour. For ellipticity β significantly larger than β_c, strong dipolar interactions force the particles to rapidly self-assemble into travelling chains. The interpretation of chaining for the general case of elliptically polarized field, $\beta \neq 0$, becomes straightforward in terms of reduced equations of motion.

In this case, the propulsion of particles can effectively be described by a time-independent single-particle potential $U_{\rm s}^{\rm eff}(x_l) = \zeta_l \langle \dot{x}_l \rangle x_l$, which is linearly dependent on the coordinate x_l and describes the individual propulsion with constant speed $\mathbf{v}_{\rm s}(\mathbf{r}_l) = \langle \dot{x}_l \rangle \hat{\mathbf{e}}_x$ along the x axis. The speed of propulsion depends on the frequency f, the ellipticity of the field, β, and the size of particle. Similarly to the case $\beta = 0$, at a low frequency $f < f_{\rm cl}(\beta)$, the particle propels with the maximum speed, $\langle \dot{x}_l \rangle = v_{\rm m}$. At high frequencies, the speed of propulsion drops down. Generally, the value of $f_{cl}(\beta)$ and the dependence of $\langle \dot{x}_l \rangle$ on f and β can be obtained only numerically. However, for frequencies f that are formally far beyond the critical value $f_{cl}(\beta)$, which represents a good approximation already for $f \gtrsim 2f_{cl}(\beta)$, we can apply the estimate $\langle \dot{x}_l \rangle_{\beta\neq 0} = \langle \dot{x}_l \rangle_{\beta=0} \sqrt{1-\beta^2}$ [28]. Here, $\langle \dot{x}_l \rangle_{\beta=0} = (v_{\rm m}/2) f_{cl}^2(0)/f^2$, which coincides with Eq. (6) considered for $f \gg f_{\rm cl}(0)$. These asymptotic results allow us to outline a rough estimate for the critical frequency at nonzero ellipticity, which would be given by $f_{cl}(\beta) \approx f_{cl}(0)(1-\beta^2)^{1/4}$.

For the dipolar interaction of particles, the full potential as in Eq. (2) can be replaced by its reduced counterpart, see Eq. (34) in Ref. [28]:

$$U_{\rm dd}^{\rm eff}(\mathbf{r}_{ll'}) = \frac{\gamma_{ll'} H_0^2}{r_{ll'}^3} \left[1 - \frac{3(1+\beta)}{2} \frac{(\mathbf{r}_{ll'} \cdot \hat{\mathbf{e}}_x)^2}{r_{ll'}^2} \right]. \qquad (10)$$

Note that this approximation taken at $\beta = 0$ is in agreement with the reduced potential obtained in the context of front propagation for circularly polarized modulation, see Eq. (19) in Ref. [29] at $H_x = 0$, $H_y = 0$. This potential is always repulsive for particles moving along the landscape side by side, $x_{ll'} = 0$, and is conditionally attractive for particles moving one behind another, $y_{ll'} = 0$, provided that $\beta > -1/3$.

4.3 Tuning structure formation leading to selective chaining

We will now consider a situation in which the driving parameters are chosen in such a way that the small particles are in the subcritical (phase-locked) regime and the large particles in the supercritical (sliding) regime. First, let us fix the field amplitude to be $H_0 = 780\,\mathrm{A/m}$ and the ellipticity $\beta = -0.12$. Because the ellipticity is relatively small, $|\beta| \ll 1$, from our estimates we find that $f_{\rm c}(\beta) \approx f_{\rm c}(0)$. Taking into consideration Eq. (7), at the given value of H_0 and the estimate of $M_{\rm s}$ we find the critical frequencies for the large and small particles, $f_{\rm c}^{\rm L} \approx 15\,\mathrm{Hz}$ and $f_{\rm c}^{\rm S} \approx 42\,\mathrm{Hz}$, respectively. Now, by choosing the frequency of modulation to be $f = 30\,\mathrm{Hz}$, we ensure that the small particles will propel with the maximum speed, $\langle \dot{x}^{\rm S} \rangle = v_{\rm m}$ because $f < f_{\rm c}^{\rm S}(\beta)$, whereas the large particles are in the sliding regime and will move much slower on average, since $f > f_{\rm c}^{\rm L}(\beta)$. From Eq. (6) and a high-frequency approximation, we obtain close estimates, $\langle \dot{x}^{\rm L} \rangle \approx v_{\rm m} - v_{\rm m}\sqrt{1-(f_{\rm c}^{\rm L}/f)^2} \approx 0.134\, v_{\rm m}$ and $\langle \dot{x}^{\rm L} \rangle \approx v_{\rm m}(f_{\rm c}^{\rm L}/f)^2/2 \approx 0.125\, v_{\rm m}$. Note that both these analytic estimates are also close to the accurate value, $\langle \dot{x}^{\rm L} \rangle = \approx 0.136\, v_{\rm m}$, obtained by numerically averaging the speed of a single particle.

We are now ready to show why chaining of only large particles is achieved. As described above, there are two independent factors that govern the dynamics of particles: the interaction of particles with the field above the FGF and the dipolar interaction between the particles. The relative contribution of these factors is drastically different for small and large particles. To validate this statement, we compare the strength of dipolar interactions relative to the energy of individual interaction with the field of substrate. As follows from Eq. (10), the characteristic energy of dipolar interaction of a pair of particles moving one behind another, $y_{ll'} = 0$, $r_{ll'} = x_{ll'}$, is $U_{\rm dd}^{\rm eff}(r_{ll'}) = -\gamma_{ll'} H_0^2(1+3\beta)/(2r_{ll'}^3)$. Since the propulsion force is $\zeta_l \langle \dot{x}_l \rangle$, the characteristic energy caused by the interaction of particle l with the field of substrate can be estimated as $U_{\rm s} = \lambda \zeta_l \langle \dot{x}_l \rangle$. Therefore, for the relative energy of dipolar interaction we obtain

$$\frac{U_{\rm dd}(r)}{U_{\rm s}} = -\frac{\gamma H_0^2(1+3\beta)}{2\lambda\zeta \langle \dot{x} \rangle r^3}, \qquad (11)$$

where ζ and $\langle \dot{x} \rangle$ are to be replaced by either $\zeta^{\rm L}$ and $\langle \dot{x}^{\rm L} \rangle$ for large or $\zeta^{\rm S}$ and $\langle \dot{x}^{\rm S} \rangle$ for small particles, respectively.

The extreme cases of interactions between large and large particles (or small and small particles) with γ replaced by $\gamma^{\rm LL}$ (or $\gamma^{\rm SS}$) are shown in Fig. 3. The fact that the corresponding energies and hence the corresponding forces at contact are strongly separated indicates that only the dipolar interactions between the large particles is non-negligible. Note that a similar analysis of interactions between small and large particles shows that although these interactions are stronger than those between the small particles they are significantly smaller than the dipolar interactions between the large particles. This fact can be explained by the fact that the interaction with the field of substrate dominates the force balance for small particles, which are strongly coupled to the translating substrate potential and the dipolar coupling to other particles is negligibly small. The strength of interaction of large particles with the field of substrate is significantly weaker. Therefore the weak dipolar forces become comparable with the forces responsible for propulsion and can no longer be neglected.

As a result, the dipolar coupling strengths $\gamma^{\rm SS}$ and $\gamma^{\rm SL}$ can be set to zero and the dynamics of small and large particles is governed by the effective equations

$$\frac{d\mathbf{r}_l^{\rm S}}{dt} = v_{\rm m}\hat{\mathbf{e}}_x + \sqrt{2D^{\rm S}}\,\boldsymbol{\xi}_l, \qquad (12)$$

$$\frac{d\mathbf{r}_{l'}^{\rm L}}{dt} = \langle \dot{x}^{\rm L} \rangle \hat{\mathbf{e}}_x + \frac{1}{\zeta^{\rm L}} \sum_{l''} \mathbf{F}_{\rm dd}^{\rm LL}(\mathbf{r}_{l'l''}) + \sqrt{2D^{\rm L}}\,\boldsymbol{\xi}_{l'}, \qquad (13)$$

where $D^{\rm S} = k_{\rm B}T/\zeta^{\rm S}$ and $D^{\rm L} = k_{\rm B}T/\zeta^{\rm L}$ are diffusion constants. The dipolar force $\mathbf{F}_{\rm dd}^{\rm LL}(\mathbf{r}_{l'l''}) = -\partial_{\mathbf{r}_{l'}} U_{\rm dd}^{\rm eff}(\mathbf{r}_{l'l''})$ is evaluated from the potential in Eq. (10) with the only nonvanishing coupling strength $\gamma^{\rm LL} = (\chi^{\rm L} V^{\rm L})^2 \mu_0/(8\pi)$.

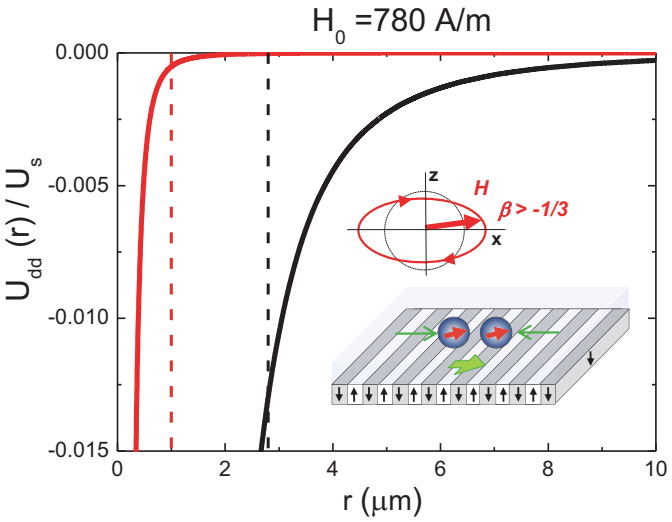

Fig. 3. Normalized magnetic dipolar interaction $U_{\rm dd}/U_{\rm s}(r)$ as given by Eq. (11) between two small (red line) and two large (black line) paramagnetic particles when subjected to an external rotating magnetic field with amplitude $H_0 = 780\,\mathrm{A/m}$ and ellipticity $\beta = -0.12$. $U_{\rm s}$ denotes the characteristic energy of interaction of the particle with the field above the FGF, which is dependent on whether the particles are in the phase-locked or in the sliding regime, see text for details. Dashed lines denote the corresponding separation distance between the particles at contact, equal to $d^{\rm S}$ for small and $d^{\rm L}$ for large particles. The schematic in the inset illustrates the geometry considered: particles having no relative displacement along the stripes display attractive dipolar interactions when the ellipticity of the rotating field $\beta > -1/3$.

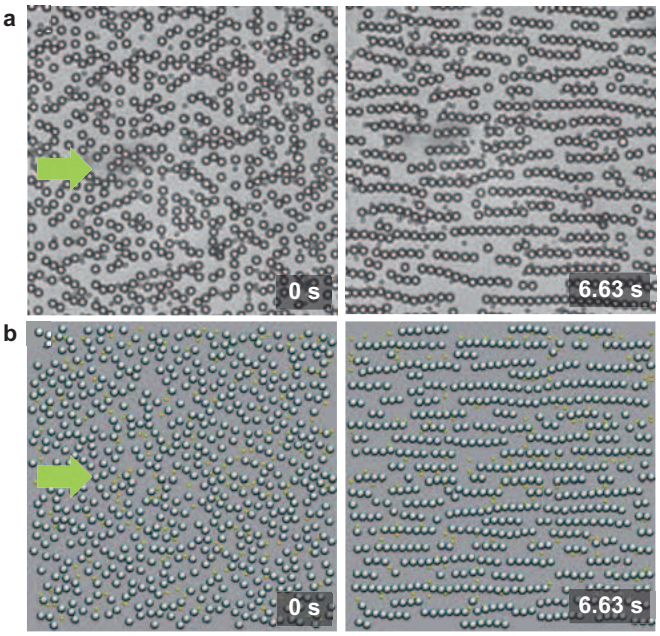

Fig. 4. (a) Optical microscope images separated by 6.63 s showing the formation of chains between only the large particles starting from an initially random mixture. The applied field has frequency $f = 30\,\mathrm{Hz}$, amplitude $H_0 = 780\,\mathrm{A/m}$ and ellipticity $\beta = -0.12$, *i.e.* the same values used in the calculation of the potential in Fig. 3. The particle net motion occurs from left to right as indicated by the green arrow. (b) Corresponding snapshot obtained from Brownian dynamics simulation of a binary mixture of paramagnetic particles driven above the FGF. The simulation based on Eqs. (12) and (13) is performed for the same values of parameters as the experiments shown in (a), and the two snapshots are separated by 6.63 s in time. The corresponding video can be found in the Supporting Information (VideoS1.wmv).

Finally, we compare the experimental and simulation results on the selective chaining process in Fig. 4. In the top panel of this image, we show two snapshots of a binary mixture of particles driven above the FGF by an elliptically polarized field with field parameters, $f = 30\,\mathrm{Hz}$, $H_0 = 780\,\mathrm{A/m}$ and $\beta = -0.12$. Starting from a random distribution of particles, after 6.63 s the large paramagnetic particles form long chains aligned across the landscape which propel to the right (along the longitudinal direction) at a certain speed, showing small thermal fluctuation in the perpendicular direction. In contrast, the small particles are transported individually between the formed chains with the maximal speed $v_{\rm m}$, without assembling in any structure during their excursion. The visual comparison with the numerical simulation using the reduced model, Eqs. (12) and (13), is displayed on the bottom panel of Fig. 4. In both cases we observe the same type of dynamics for both kinds of particles, with a clear selective process in chain formation arising from the difference in the interparticle interactions. Even by increasing the observation time, we never detect any signature of chaining for the small particles, which is attributed to trapping by the travelling potential, dominating over the effects of the dipolar interactions. The corresponding video, illustrating the dynamics of the binary mixture of particles in the experiment and simulation, can be found in the Supporting Information (VideoS1.wmv).

5 Conclusions

To summarize, we have studied the dynamics of a binary mixture of interacting paramagnetic colloidal particles in a travelling spatially periodic potential. A sinusoidal landscape is generated by using a magnetic structured substrate. Being additionally subjected to a temporal modulation in the form of a rotating magnetic field, the periodic landscape starts to move with the speed proportional to the frequency of modulation, which causes the particles to propel. Upon suitable choice of the field parameters, we show that selective chaining process can be induced by forcing one type of particle to assemble into condensed structures which laterally confine the motion of the smaller particles.

The selective chaining process can be used to generate remotely controllable colloidal channels, confining the flow of smaller magnetic particles [30], which presents a mesoscopic model system for transport in a microfluidic medium. Furthermore, of interest is the behaviour of the system at higher densities and in particular how different relative fractions of particles affect transport characteristics. More in general, binary mixture of particles driven by an external field have been investigated theoretically [31,32,33,34,35,36] and experimentally [20,37] by different research groups. Possible applications include size segregation of magnetic species, fractionation in lab-on-a-chip devices or transport of biological species in analytic devices.

P. T. acknowledges support from the ERC Starting Grant "DynaMO" (no. 335040), from Mineco (No. RYC-2011-07605 and No. FIS2013-41144-P) and AGAUR (Grant No. 2014SGR878). A. V. S. and P. T. acknowledge support from a bilateral German-Spanish program of DAAD (project no. 57049473) via the Bundesministerium für Bildung und Forschung (BMBF). A. V. S. acknowledges P. T. and the Departament de Física de la Matèria Condensada for hosting him as a visiting scientist at the University of Barcelona.

References

1. E. Mirowski, J. Moreland, A. Zhang, S. E. Russek, M. J. Donahue, Appl. Phys. Lett. **86**, 243901 (2005).
2. Q. Ramadana, Y. Chen, V. Samper, D. P. Poenar, Appl. Phys. Lett. **88**, 032501 (2006).
3. K. Gunnarsson, P. E. Roy, S. Felton, J. Pihl, P. Svedlindh, S. Berner, H. Lidbaum, S. Oscarsson, Adv. Mater. **17**, 1730 (2005).
4. B. B. Yellen, O. Hovorka and G. Friedman, Proc. Natl. Acad. Sci. U. S. A. **102**, 8860 (2005).
5. P. Tierno, S. V. Reddy, T. H. Johansen and T. M. Fischer, Phys. Rev. E **75**, 041404 (2007).
6. M. Donolato, P. Vavassori, M. Gobbi, M. Deryabina, M. F. Hansen, V. Metlushko, B. Ilic, M. Cantoni, D. Petti, S. Brivio, R. Bertacco, Adv. Mater. **22**, 2706 (2010).
7. T. Henighan, D. Giglio, A. Chen, G. Vieira, and R. Sooryakumar, Appl. Phys. Lett. **98**, 103505 (2011).
8. A. Ehresmann, D. Lengemann, T. Weis, A. Albrecht, J. Langfahl-Klabes, F. Gollner, and D. Engel, Adv. Mater. **23**, 5568 (2011).
9. M. A. Gijs, F. Lacharme and U. Lehmann, Chem Rev. **110**, 1518 (2010).
10. J. E. Martin, A. Snezhko, Rep. Prog. Phys. **76**, 126601 (2013).
11. M. Zborowski, J. J. Chalmers, Magnetophoresis: Fundamentals and Applications, Wiley Encyclopedia of Electrical and Electronics Engineering, 123 (2015).
12. M. Suwa, H. Watarai, Anal Chim Acta. **690**, 137 (2011).
13. L. E. Helseth, T. Backus, T. H. Johansen, and T. M. Fischer, Langmuir **21**, 7518 (2005).
14. P. Tierno, T. M. Fischer, T. H. Johansen, F. Sagués, Phys. Rev. Lett. **100**, 148304 (2008).
15. P. Tierno, P. Reimann, T. H. Johansen, F Sagués, Phys. Rev. Lett. **105**, 230602 (2010).
16. P. Tierno, Phys. Rev. Lett., **109**, 198304 (2012).
17. A. V. Straube, P. Tierno, Europhys. Lett., **103**, 28001 (2013).
18. P. Tierno, S. V. Reddy, M. G. Roper, T. H. Johansen, T. M. Fischer, J. Phys. Chem. B **112**, 3833 (2008).
19. P. Tierno, A. Soba, T. H. Johansen, F. Sagués, Appl. Phys. Lett. **93**, 214102 (2008).
20. B. B. Yellen, R. M. Erb, H. S. Son, R. Hewlin Jr., H. Shang, and G. U. Lee, Lab Chip **7**, 1681 (2007).
21. P. Tierno, F. Sagues, T. H. Johansen, T. M. Fischer, Phys. Chem. Chem. Phys. **11**, 9615 (2009).
22. L. Clime, B. L. Drogoff, T. Veres, IEEE Trans. Magn. **43**, 2929 (2007).
23. L. E. Helseth, J. Phys. D: Appl. Phys. **40**, 3030 (2007).
24. P. Tierno, Soft Matter **8**, 11443 (2012).
25. J. C. Crocker, D. G. Grier, J. Colloid Interface Sci., **179**, 298 (1996).
26. H. Carstensen, V. Kapaklis and M. Wolff, Phys. Rev. E, **92**, 012303 (2015).
27. S. Lacis, J. C. Bacri, A. Cebers and R. Perzynski, Phys. Rev. E **55**, 2640 (1997).
28. A. V. Straube, P. Tierno, Soft Matter **10**, 3915 (2014).
29. F. Martinez-Pedrero, P. Tierno, T. H. Johansen, A. V. Straube, Scientific Reports **6**, 19932 (2016).
30. T. O. E. Skinner, S. K. Schnyder, D. G. A. L. Aarts, J. Horbach, and R. P. A. Dullens, Phys. Rev. Lett. **111**, 128301 (2013).
31. J. Dzubiella, G. P. Hoffmann, H. Löwen, Phys. Rev. E **65**, 021402 (2002).
32. J. Dzubiella, H. Löwen, J. Phys.: Condens. Matter **14**, 9383 (2002).
33. C. Reichhardt, C. J. Olson Reichhardt, Phys. Rev. E **74**, 011403 (2006).
34. A. Wysocki, H. Löwen, Phys. Rev. E **79**, 041408 (2009).
35. D. Speer, R. Eichhorn, P. Reimann, Phys. Rev. Lett. **105**, 090602 (2009).
36. R. Lugo-Frias, S. H. L. Klapp, J. Phys. Condensed Matter (2016), in press (arXiv:1511.07691).
37. T. Vissers, A. van Blaaderen, A. Imhof, Phys. Rev. Lett. **106**, 228303 (2011).